Theoretical Development of a Magnetic Force and an Induced Motion in Elastic Media for a Magneto-Motive Technique

In Gweon Lim

Department of Mechanical Engineering, Myong-Ji University, Yongin 17058, Korea

Suhyun Park

Department of Biomedical Engineering, University of Texas at Austin, TX 78712, USA

Junghwan Oh*

Department of Biomedical Engineering, Pukyong National University, Busan 48513, Korea

The theoretical development of a magnetic force and an induced motion while applying a magnetic field to magnetic nanoparticles in elastic media is described. An analytical expression for tissue-surface displacement derived from Mindlin's theory of elasticity in semi-infinite media was used to analyze the magneto-motive technique. The initial motion of the magnetic nanoparticles is driven by a constant magnetic force that displays a dampened transient motion before steady-state movement at twice the modulation frequency of the applied sinusoidal magnetic field. The motion of the nanoparticles at double the modulation frequency originated from the magnetic force being proportional to the product of the magnetic flux density and its gradient. Finally, we demonstrate the detection of iron-oxide nanoparticles taken up by liver parenchymal Kupffer cells and macrophages in atherosclerotic plaques by using a differential-phase optical coherence tomography (DP-OCT) system to compare simulation results with experimental data.

I. INTRODUCTION

Magnetic nanoparticles have been studied intensively over the past decade for use as contrast agents in magnetic resonance imaging [1] and are considered as promising candidates for various applications combining diagnosis, imaging, and therapy. More recently, magnetic nanoparticle probes have been expanded for numerous novel biomedical applications, such as reagents for cell labelling [2], cell tracking [3], drug delivery [4], cell separation [5], and treatment of cancer [6, 7]. Recently, there has been increased interest in the development of highly susceptible magnetic probes and contrast mechanisms appropriate for molecular imaging and biomedical applications. A magneto-motive technique using mechanically- applied time-varying or pulsed magnetic forces to a specific tissue induces a small displacement of particles in the surrounding tissue, which can be detected or imaged using traditional imaging modalities, such as optical coherence tomography (OCT) [8, 9], ultrasound (US) [10], laser speckle imaging (LSI) [11], and photoacoustic tomography (PAT) [12].

Examination of the sentinel lymph nodes (SLNs), the first lymph nodes that drain primary tumors and the primary site reached by metastasizing cancer cells, plays an important role in the diagnosis and treatment of cancer. Recently, both frequency- and phase-gated magneto-motive ultrasound (MM-US) has been used to image SLNs in prior staging using magnetic nanoparticles [13]. Magneto-motive photoacoustic (MM-PA) imaging is a newly developed technique to increase the sensitivity and specificity of targeted lesions compared to conventional photoacoustic imaging. MM-PA, when it incorporates the use of multiple contrast agents and magnetic manipulations [14], dramatically reduces background noise from strong optical absorbers, such as blood and tissue. To overcome the inherent limitations of small tissue-restoring forces and the slow acquisition speed of magneto-motive optical coherence tomography(MM-OCT), a dual coil magnetic generator was developed that utilized a higher frequency (> 500 Hz) to reduce interference from the low-frequency signals generated from the intrinsic heartbeat, the pulsation of blood vessels, and

*E-mail: jungoh@pknu.ac.kr; Fax: +82-51-629-5779

Magnetic Field on Nanoparticle (SPIO, MION) (Table 1)

Magnetic Force on Nanoparticle (Figure 3, Equation 3)

$$\mathbf{F} = -\nabla U = \nabla(\frac{\chi_s V}{2u_0}|\mathbf{B}|^2) = \chi_s V \nabla(\frac{|\mathbf{B}|^2}{2u_0})$$

Motion of Nanoparticles using Laplace Transform (Equation 16)

$$s^2 Z_{np}(s) + \frac{r}{m} s Z_{np}(s) + \frac{k}{m} Z_{np}(s) = \frac{a}{s} - \frac{as}{(s^2 + \omega_B^2)}$$

Transient Motion of Nanoparticle (Figure 5)

Steady State Motion of Nanoparticle (Figure 5)

Motion of Nanoparticle (Figure 4, Equation 12)

$$\frac{\partial^2 z_{np}(t)}{\partial t^2} + \gamma \frac{\partial z_{np}(t)}{\partial t} + \omega_0^2 z_{np}(t) = a[1 - \cos(\omega_B t)]$$

Tissue Surface Displacement in Elastic Media Using Galerkin Vector: (Equation 31)

$$W = \left[\frac{P}{16\pi G(1-v)}\right]\left\{\frac{3-4v}{R_1} + \frac{8v^2 - 12v + 5}{R_2} + \frac{(z-c)^2}{R_1^3} + \frac{(3-4v)(z+c)^2 - 2cz}{R_2^3} + \frac{6cz(z+c)^2}{R_2^5}\right\}$$

Steady-State Motion of Nanoparticle (SPIO, MION): (Figure 4, Equation 15)

$$z_{np}(t) = z_{0,ss} e^{i\omega_B t} = \frac{-a e^{i\omega_B t}}{\left[\omega_B^2 + i\gamma\omega_B + \omega_0^2\right]}$$

Tissue Surface Displacement in Elastic Media (Figure 7, Equation 33)

$$z_z(t) = \left[\frac{m\ddot{z}_{np}}{16\pi G(1-v)}\right]\left\{\frac{3-4v}{R_1} + \frac{8v^2 - 12v + 5}{R_2} + \frac{(z-c)^2}{R_1^3} + \frac{(3-4v)(z+c)^2 - 2cz}{R_2^3} + \frac{6cz(z+c)^2}{R_2^5}\right\}$$
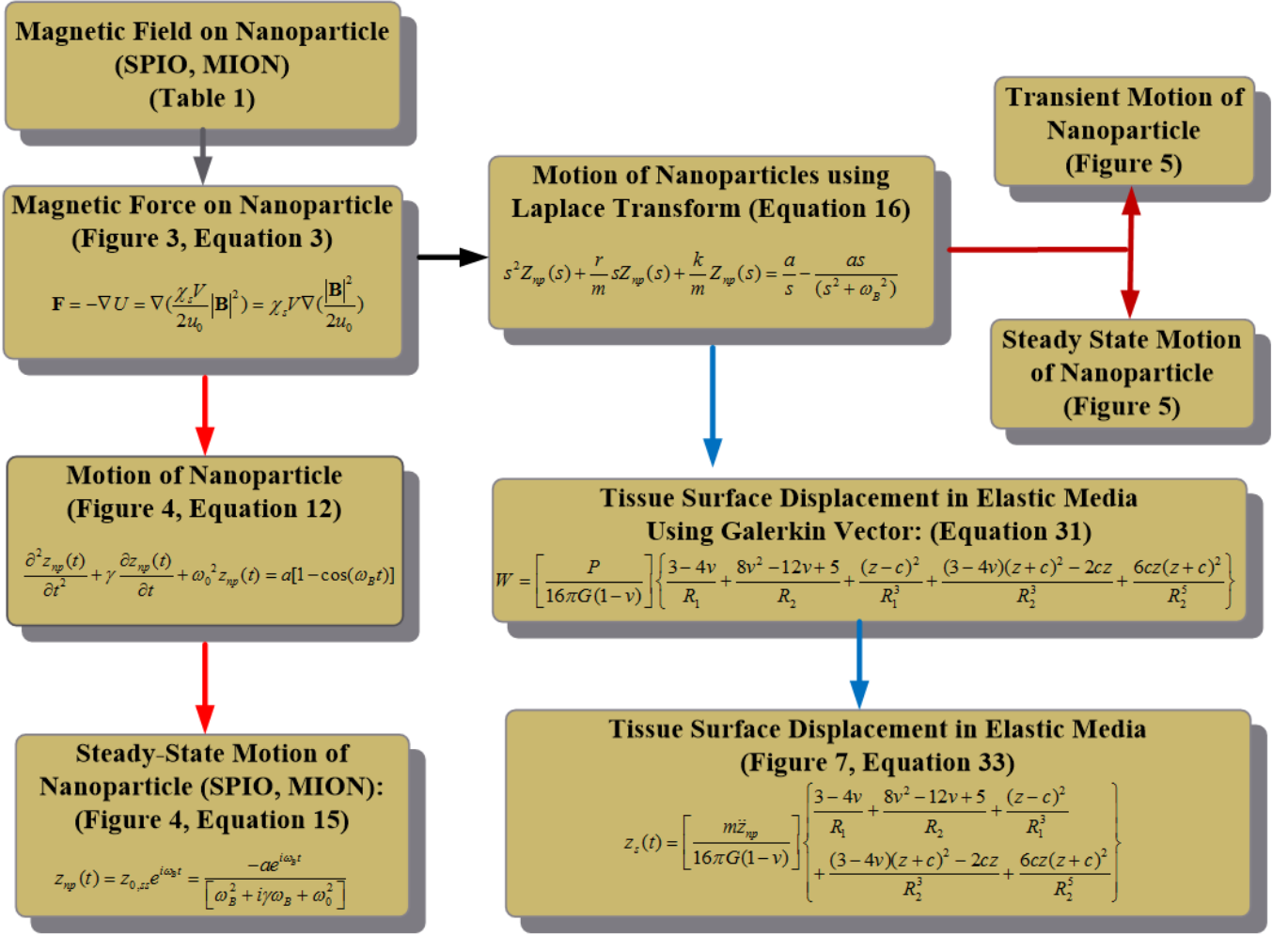
Fig. 1. (Color online) Outline of the theoretical model of magnetic force acting on magnetic nanoparticles in elastic media.

muscle twitching within the body [15].

Most previous investigations using magneto-motive techniques have demonstrated the ability to identify magnetically-labelled cells in phantom studies using various imaging modalities. Because the particles used in this technique are on the nanoscale order, and thus are at the sub-resolution level, we cannot resolve them individually, but rather we can detect their aggregate responses and how they displace structures (e.g., cells and organelles) within their microenvironments.

For the demonstration of a magnetic force acting on magnetic nanoparticles, fiber-based dual-channel differential-phase optical coherence tomography (DP-OCT), which is capable of high path-length sensitivity, is able to detect an optical path-length change (Δp) with nanometer resolution between discrete reflecting surfaces. DP-OCT has been applied to the phase-contrast imaging of cells, the measurement of nanometer-scale displacement changes corresponding to neuronal activity without application of chemicals, the electro-kinetic response of cartilage samples to an external current, the

photo-thermal response of tissue damage, and changes in analyte concentrations [16]. Figure 1 summarizes this paper, illustrating the theoretical development of the magnetic force and motion induced by the application of a magnetic force to magnetic nanoparticles, and presents a tissue-surface displacement equation derived from Mandlin's elasticity theory in a semi-infinite model.

II. METHODS

1. Magnetic Field Effect on the Magnetic Nanoparticles

Table 1 illustrates the commercially-available magnetic nanoparticles, as classified by their overall size and surface coating. Magnetic nanoparticles can be divided into three different categories: 1) standard superparamagnetic iron oxide (SPIO), ranging from 60 ~ 150 nm; 2) ultra-small SPIO (USPIO), ranging from 10 ~ 40

Table 1. Classification of SPIO nanoparticles [1,6,17].

Agent	Class	Trade and common names	Status	Mean size
AMI-121	Oral SPIO	Lumirem, Gastromark, Ferumoxsil	Approved	> 300 nm
OMP	Oral SPIO	Abdoscan	Approved	$3.5\ \mu$m
AMI-25	SPIO	Feridex, Endorem, Ferumoxide	Approved	$80 \sim 150$ nm
SHU555A	SPIO	Resovist	Phase III	62 nm
AMI-227	USPIO	Sinerem, Combidex, Ferumoxtran	Phase III	$20 \sim 40$ nm
NC100150	USPIO	Clariscan	Phase II	20 nm
CODE 7228	USPIO	(Advanced Magnetics)	Phase II	$18 \sim 20$ nm
MION-46	MION	MION46 (manufactured by CMIR)	-	$20 \sim 25$ nm
MION-47	MION	MION47 (manufactured by CMIR)	-	27.5 nm
MION-48	MION	MION48 (manufactured by CMIR)	-	$20 \sim 25$ nm

Table 2. Properties and applications of super-paramagnetic nanoparticles [1].

Agent	Class	Target Organs	Dose	Reference
AMI-121	Oral SPIO	GI lumen	$1.5 \sim 3.9$ mmol/Fe	[30]
OMP	Oral SPIO	GI lumen	0.5 g/l $(400 - 600$ ml)	[31]
AMI-25	SPIO	Liver / Spleen	$15\ \mu$mol Fe/kg	[32]
SHU555A	SPIO	7 Liver / Spleen	$8\ \mu$mol Fe/kg	[32–34]
		Perfusion	$4 \sim 16$ mol Fe/kg	
		MRA	$10\ \mu$mol Fe/kg	
AMI-227	USPIO	Lymph nodes	$30 \sim 45\ \mu$mol Fe/kg	[35–38]
		MRA	$14 \sim 30$ mol Fe/kg	
NC100150	USPIO	Perfusion	$7\ \mu$mol Fe/kg	[22]
		MRA	$50 \sim 100$ mol Fe/kg	[39]
CODE 7228	USPIO		μmol Fe/kg	
MION	MION	Liver	μmol Fe/kg	[3,6,21,40]
		Atherosclerosis	μmol Fe/kg	

nm, and; 3) monocrystalline iron oxide (MION, a subset of USPIO), ranging from $10 \sim 30$ nm [17]. Table 2 illustrates the properties and applications of super-paramagnetic iron-oxide nanoparticles, including SPIO, USPIO, and MION.

To evaluate the force acting on magnetic nanoparticles, we used the magnetic energy for this analysis [18], as indicated by the following equation:

$$U = -\frac{1}{2}\mathbf{m} \cdot \mathbf{B}. \tag{1}$$

If a magnetic material is exposed to an external magnetic flux density, $\mathbf{B}$, individual nanoparticles have an overall response determined by the magnetic moment, m, and the viscoelastic properties of the surrounding material, including tissue and cells. The magnetic flux density on magnetic nanoparticles may be written as the following:

$$\mathbf{B} = \mu_0(\mathbf{H} + \mathbf{M}), \tag{2}$$

where $\mu_0(4\pi \times 10^{-7}$ H/m) is the permeability of free space (SI unit: $4\pi \times 10^{-7}$ N/A^2), $\mathbf{M}$ is the magnetic moment per unit volume, and $\mathbf{H}$ is the magnetic field strength. The magnetic moment, m, within the volume, V, is given by $m = \mathbf{M}V$.

The Magnetization of magnetic particles can be classified in terms of the standard relation $\mathbf{M} = \chi\mathbf{H}$. The magnetic susceptibility (χ) is proportional to the number of magnetic particle atoms in the tissue and the square of the magnetic moment. In practice, the magnetization $\mathbf{M}$ is not linearly proportional to magnetic field strength $\mathbf{H}$ after saturation of the magnetic field (usually over $2 - 3$ Tesla). This nonlinear relationship between the magnetization induced on a paramagnetic material and the applied magnetic field strength is represented by using the Langevin function [19,20]:
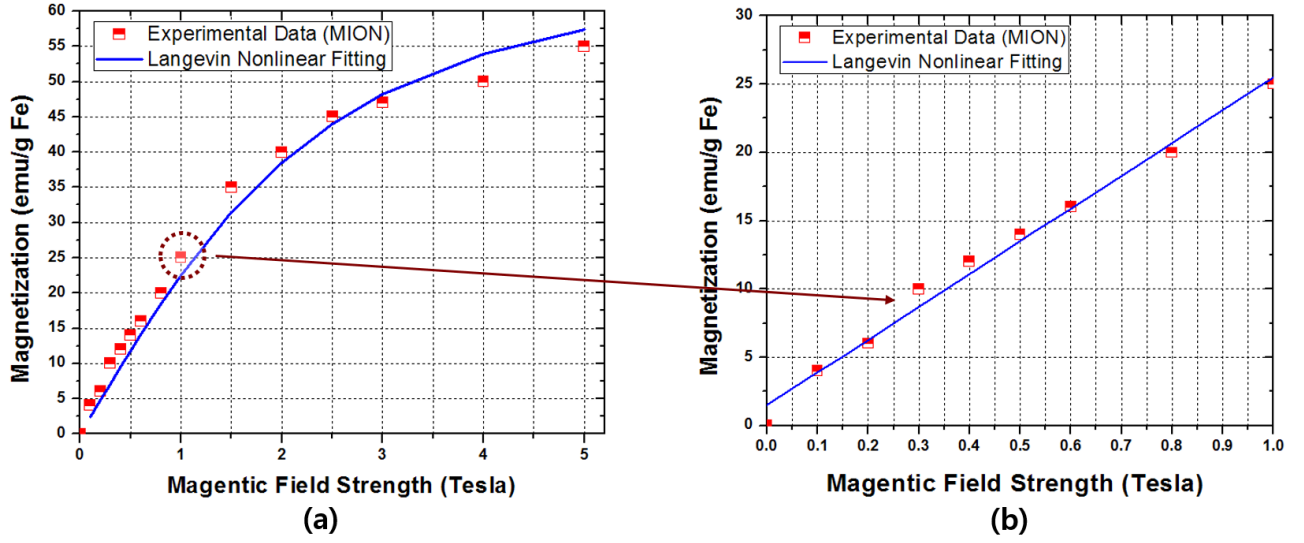
Fig. 2. (Color online) Magnetization expressed as a function of the magnetic-field strength for MION nanoparticles at room temperature. The solid line was fitted to the data by using a Langevin nonlinear function at a magnetic field of (a) $0-5$ Tesla and (b) $0-1$ Tesla [26].

$$
\begin{aligned}
\mathbf{M(H)} &= Nm\left[\coth\left(\frac{\mu_0 m\mathbf{H}}{kT}\right) - \left(\frac{kT}{\mu_0 m\mathbf{H}}\right)\right] \\
&\cong Nm\left[\frac{1}{3}\frac{\mu_0 m\mathbf{H}}{kT} - \frac{1}{45}\left(\frac{\mu_0 m\mathbf{H}}{kT}\right)^3 + \frac{2}{945}\left(\frac{\mu_0 m\mathbf{H}}{kT}\right)^5 + \cdots\right] \\
&\cong \frac{Nm^2\mu_0\mathbf{H}}{3kT}\left[1 - \frac{1}{15}\left(\frac{\mu_0 m\mathbf{H}}{kT}\right)^2 + \frac{2}{315}\left(\frac{\mu_0 m\mathbf{H}}{kT}\right)^4 + \cdots\right] \\
&\cong \frac{Nm^2\mu_0}{3kT}\mathbf{H},
\end{aligned}
\tag{3}
$$

where

Langevin function, $L(x) = \coth(x) - 1/x$
N = the number of atoms per unit volume
m = the magnetic moment per atom
   (4.47×10^{-8} erg/G)
k = Boltzman's constant
   (1.3807×10^{-16} erg K^{-1} = 1.3807×10^{-23} JK^{-1})
μ_0 = Permeability of free space ($4\pi \times 10^{-7}$ H/m)
T = Kelvin temperature (300 K).

Once the constants, m, k, μ_0, and T have been determined, the total number of Fe atoms (N = 1.4076 $\times$ 10^9) is calculated by nonlinear fitting (Fig. 2) of MION magnetization data recorded by Shen *et al.* [21].

The Langevin function clearly represents a nonlinear magnetization curve relationship between the magnetization and the magnetic field strength for MION nanoparticles over the entire magnetic field range of $0-5$ Tesla, as illustrated in Fig. 2(a). At low magnetic fields ($0-1$ Tesla), the magnetization curve for MION nanoparticles

is directly proportional to the magnetic field strength, as shown by the linear fitting of the data (Fig. 2(b)). After the magnetic field strength (H) reaches a value of 1.5 Tesla, the magnetization increases very slowly and becomes saturated when H is near or over 2 Tesla. In clinical magnetic resonance imaging (MRI), the detectable sensitivity of iron nanoparticles was reported at 50 nmol Fe/g tissue [21]. In preliminary experiments, MION was used to demonstrate cellular uptake of nanoparticles by macrophages (1 mg Fe/10^6 cells) with 1.5×10^6 MION particles/cell [22]. Table 3 shows the magnetic susceptibility of SPIO and MION nanoparticles in CGS units [23].

The magnetization of magnetic particles can be classified in terms of the standard relation $\mathbf{M} = \chi\mathbf{H}$. Therefore, the induced magnetic moment m becomes:

$$\mathbf{m} = \mathbf{M}V = \chi V\mathbf{H} = \chi V\mathbf{B}/u_0, \tag{4}$$

$$\mathbf{B} = \mu_0(\mathbf{H} + \chi\mathbf{H}) = \mu_0\mu_R\mathbf{H} = \mu\mathbf{H}, \tag{5}$$

where μ_R is defined as the relative permeability given

Table 3. Magnetic susceptibility of SPIO and MION.

	SPIO	MION
	CGS UNIT	CGS UNIT
χ	(Dimensionless)	(Dimensionless)
	0.89×10^{-2}	1.58×10^{-2}
$\chi_g = \frac{\chi}{\rho}$	cm³/g	cm³/g
	7.16×10^{-3}	2×10^{-3}
$\chi_M = \frac{\chi W_{iron}}{\rho}$	cm³/mol Fe	cm³/mol
	0.4 ± 0.02	0.112 ± 0.008

Fig. 3. (Color online) Magnetic force acting on SPIO and MION nanoparticles.

a simple relationship (Eq. (5)) between **B** and **H** ($\mathbf{B} = \mu\mathbf{H}$). The susceptibility of the magnetic nanoparticles χ is dimensionless in SI units and given by magnetic dipole density for each paramagnetic material, which is essential for characterizing the magnetic properties of magnetic nanoparticles. From Eq. (1), the magnetic energy U of a SPIO nanoparticle in an external magnetic field is given by:

$$U = -\frac{1}{2}\mathbf{m} \cdot \mathbf{B} = -\frac{\chi_s V}{2u_0}|\mathbf{B}|^2. \tag{6}$$

The magnetic force acting on SPIO nanoparticles becomes

$$\begin{aligned}\mathbf{F} &= -\nabla U = \nabla\left(\frac{\chi_s V}{2u_0}|\mathbf{B}|^2\right) \\ &= \chi_s V \nabla\left(\frac{|\mathbf{B}|^2}{2u_0}\right) = \chi_s V \nabla\left(\frac{1}{2}\mathbf{B} \cdot \mathbf{H}\right),\end{aligned} \tag{7}$$

where $\frac{1}{2}\mathbf{B}\cdot\mathbf{H}$ = the magnetic static field energy density [24]. We assume in our analysis a sinusoidal magnetic flux density that is principally along the z-direction. Hence, we write $\overrightarrow{\mathbf{B}}(x,y,z;t) = \sin(2\pi f_n t)B_z(z)\hat{k}$ and the magnetic force $\mathbf{F_m}$ acting on nanoparticles as

$$\mathbf{F_m} = \frac{\chi_s V_s}{2\mu_0}[1 - \cos(4\pi f_n t)]\mathbf{B}_z(z)\frac{\partial\mathbf{B}_z}{\partial z}, \tag{8}$$

where f_n is the modulation frequency of the applied sinusoidal magnetic field used in the magneto-motive technique.

The magnetic force on a single nanoparticle can be calculated by using Eq. (7) and magnetic susceptibility data from Table 2. The mass density of iron, $\rho_{spio} = 5.18$ (g/cm³), and the molar mass of iron, $MW_{spio} = 231.55$ (g/mol), were used to calculate the magnetic force on each nanoparticle. The magnetizations of MION (2.8 nm $\pm$ 0.9 $\sim$ 4.6 nm $\pm$ 1.2) [25] and SPIO nanoparticles were reported as 38.9 emu/g iron at 2 Tesla and 63.7 emu/g iron at 1.5 Tesla, respectively [26]. To calculate the magnetic force acting on the magnetic nanoparticle, we used the mean molecular weights of SPIO (2000 kDa) and MION (38.9 kDa). Figure 3 shows the simulation results for the maximum magnetic forces acting on SPIO
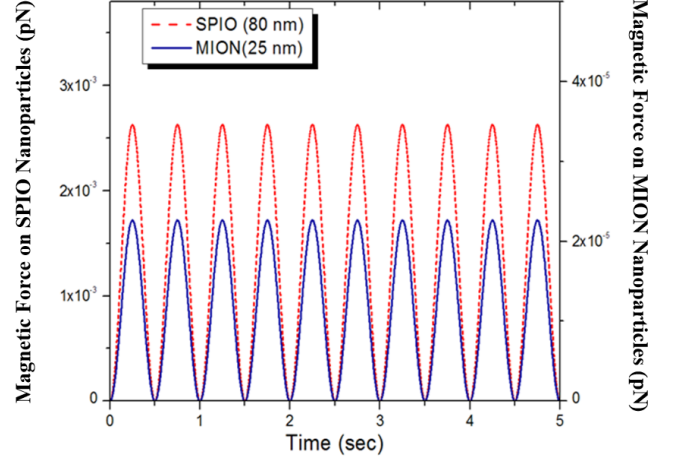
(2.6283×10^{-15} (N)) and MION (2.263×10^{-17} (N)) nanoparticles.

III. RESULTS

1. Magnetic Nanoparticle Dynamics: Steady State

The total force acting on nanoparticles in the z-direction can be written as

$$\sum\mathbf{F}_z = m\frac{\partial^2 z}{\partial t^2} = \mathbf{F_m} - kz_{np}(t) - r\frac{\partial z_{np}}{\partial t}, \tag{9}$$

where $kz_{np}(t)$ is an elastic restoring force, and $r\frac{\partial z_{np}}{\partial t}$ is a drag force that accounts for the viscous properties of the local tissue environment. The negative signs of the viscous drag and restoring forces indicate that these forces are in the opposite direction to the nanoparticle movement, $z_{np}(t)$. We can write second-order differential equations of motion by dividing by the mass m:

$$\begin{aligned}&\frac{\partial^2 z_{np}(t)}{\partial t^2} + \frac{r}{m}\frac{\partial z_{np}}{\partial t} + \frac{kz_{np}(t)}{m} \\ &= \frac{\chi V}{2m\mu_0}[1 - \cos(4\pi f_n t)]\mathbf{B}_z(z)\frac{\partial\mathbf{B}_z(z)}{\partial z}.\end{aligned} \tag{10}$$

Eq. (10) can be rewritten using the first terms in the Maclarin series for the magnetic field and its gradient:

$$\begin{aligned}&\frac{\partial^2 z_{np}(t)}{\partial t^2} + \frac{r}{m}\frac{\partial z_{np}}{\partial t} + \frac{kz_{np}(t)}{m} \\ &\cong \frac{\chi V}{2m\mu_0}[1 - \cos(4\pi f_n t)]\mathbf{B}_z(z)\frac{\partial\mathbf{B}_z(0)}{\partial z}.\end{aligned} \tag{11}$$

Letting $a = \frac{\chi_s V_s}{2m\mu_0}\mathbf{B}_z(0)\frac{\partial\mathbf{B}_z(0)}{\partial z}$, $\omega_B = 4\pi f_n$, $k/m = \omega_0^2$, and $r/m = \gamma$, the second-order differential equation,
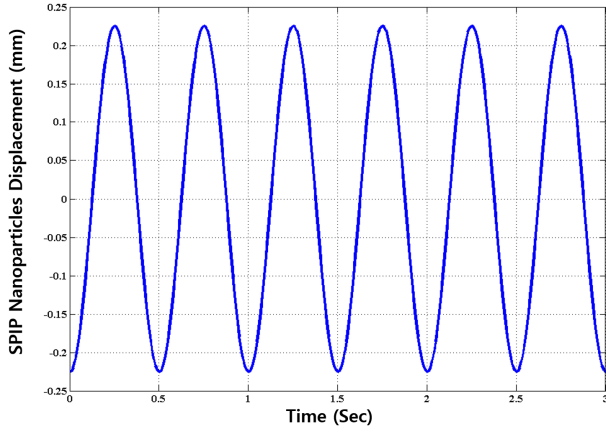
Fig. 4. (Color online) Simulated results for the motion of SPIO nanoparticles subjected to a magnetic force of 2 Tesla at 1 Hz.

Eq. (11), may be rewritten as

$$\frac{\partial^2 z_{np}(t)}{\partial t^2} + \gamma \frac{\partial z_{np}(t)}{\partial t} + \omega_0^2 z_{np}(t) = a[1 - \cos(\omega_B t)]. \quad (12)$$

In the case of steady-state motion, $z_{np}(t) = z_{0,ss}e^{i\omega_B t}$ is introduced to obtain an oscillating displacement of nanoparticles. $z_{0,ss}$ represents the displacement of magnetic nanoparticles in the steady state, and the induced displacement of nanoparticles may, therefore, be express as

$$\frac{\partial^2 z_{0,ss}e^{i(\omega_B)t}}{\partial t^2} + \frac{\partial z_{0,ss}e^{i(\omega_B)t}}{\partial t} + \omega_0^2 z_{0,ss}e^{i(\omega_B)t}$$
$$= -ae^{i(\omega_B)t}. \quad (13)$$

Eq. (13), thus, becomes

$$[(i\omega_B)^2 + \gamma(i\omega_B) + \omega_0^2]z_{0,ss} = -a, \quad (14)$$

$$z_{np}(t) = z_{0,ss}e^{i\omega_B t} = \frac{-ae^{i\omega_B t}}{[\omega_B^2 + i\gamma\omega_B + \omega_0^2]}. \quad (15)$$

In Eq. (15), $z_{np}(t)$ represents the nanoparticle's movement in the steady state corresponding to our measurement of tissue surface displacement. In the case of steady-state conditions, the displacement of nanoparticles a magnetic field strength of 2 Tesla and the frequency of 1 Hz illustrated as shown in Fig. 4.

2. Magnetic Nanoparticle Dynamics: transient and steady states

To understand the overall mechanisms of nanoparticle displacement, one can use Laplace transform to solve the second-order differential equation, Eq. (12). Assuming zero initial displacements and velocity, we find the following:

$$s^2 Z_{np}(s) + \frac{r}{m}s Z_{np}(s) + \frac{k}{m}Z_{np}(s) = \frac{a}{s} - \frac{as}{(s^2 + \omega_B^2)},$$

$$Z_{np}(s) = \frac{\frac{a}{s} - \frac{as}{(s^2+\omega_B^2)}}{(s^2 + \gamma s + \omega_0^2)} \quad (16)$$

$$= a\left(\frac{1}{(s^2 + \gamma s + \omega_0^2)s} - \frac{s}{(s^2 + \gamma s + \omega_0^2)(s^2 + \omega_B^2)}\right).$$

If $4\omega_0^2 - \gamma^2 > 0$, we can write the nanoparticle movement $(z_{np}(t))$ by computing the sum of the transforms:

$$z_{np}(t) = \frac{a\left[\begin{array}{l} -\gamma\omega_B\omega_0^2\sin(\omega_B t) + (\gamma^2\omega_B^2 - 2\omega_B^2\omega_0^2 + \omega_B^4 + \omega_0^4) \\ -\omega_0^4\cos(\omega_B t) + (\omega_B^2\omega_0^2)\cos(\omega_B t) + \\ \exp\left(-\frac{1}{2}\gamma t\right)\left(\begin{array}{l} -\omega_B^2(\gamma^2 + \omega_B^2 - \omega_0^2)\cos\left(\frac{1}{2}t(4\omega_0^2 - \gamma^2)^{\frac{1}{2}}\right) \\ \frac{-\omega_B^2\gamma(-3\omega_0^2 + \omega_B^2 + \gamma^2)\sin\left(\frac{1}{2}t(4\omega_0^2 - \gamma^2)\right)}{(4\omega_0^2 - \gamma^2)^{\frac{1}{2}}} \end{array}\right) \end{array}\right]}{(\omega_0^2(\gamma^2\omega_B^2 - 2\omega_b^2\omega_0^2 + \omega_B^4 + \omega_0^4))}. \quad (17)$$

We find the displacement $z_{np}(t)$ of nanoparticles by using an inverse Laplace transform; the solution includes both transient and steady-state terms. The initial motion of magnetic nanoparticles is driven by a constant magnetic force and displays a damped transient motion before steady-state motion dominates at twice the modulation frequency of the applied sinusoidal magnetic field. The motion of the nanoparticles at double the modulation frequency originates from the magnetic force being proportional to the product of the magnetic flux density
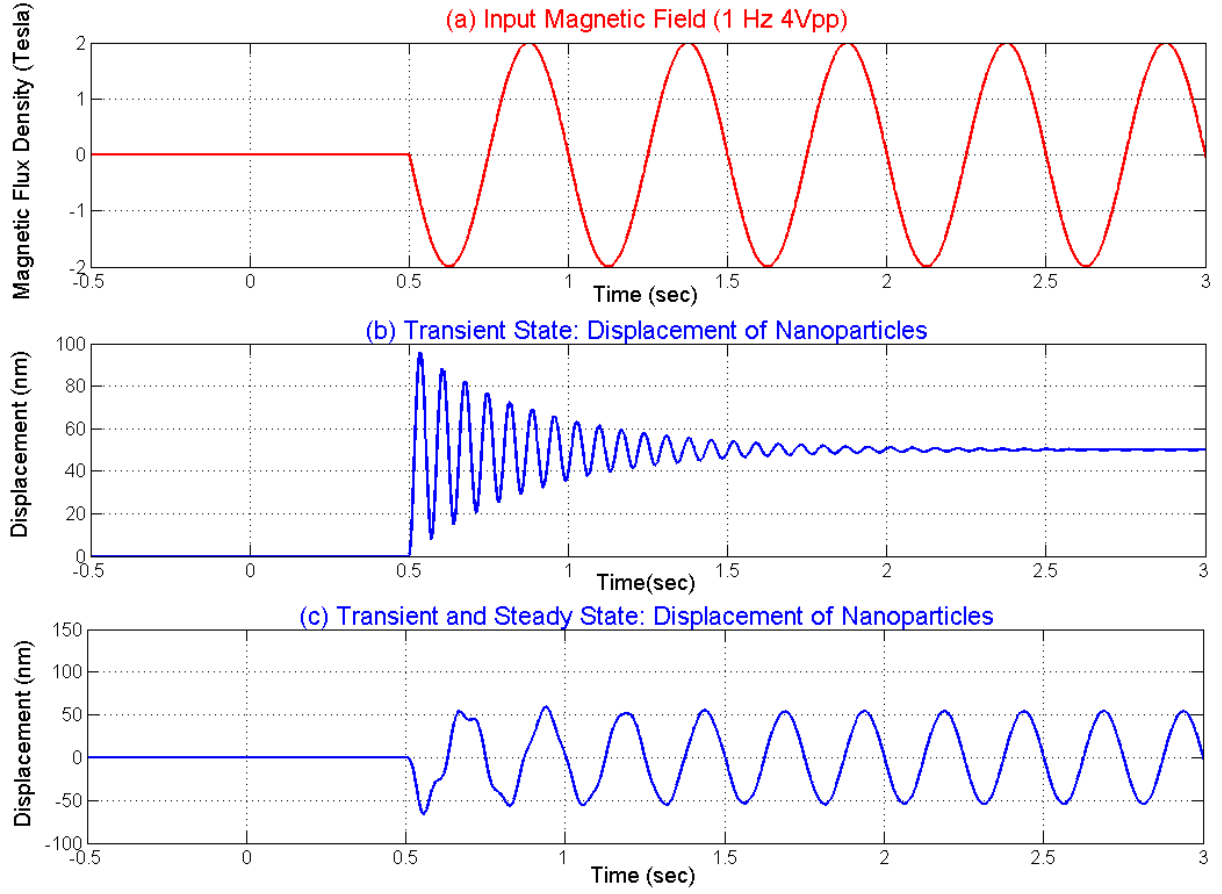
Fig. 5. (Color online) Simulation results for nanoparticle displacement driven by an external magnetic field: (a) external magnetic flux density, (b) transient movement, and (c) steady-state movement.

and the gradient (Eq. (8)).

Figure 5 illustrates the simulation result of nanoparticle displacement driven by an external magnetic field (panel (a)), giving transient motion (panel (b)), and steady-state motion (panel (c)), as determined by using an inverse Laplace transform of Eq. (16). The frequency of the transient motion is larger than that of the steady state motion. The larger displacements at initial times are due to a transient effect, as steady-state displacements are seen to be twice the frequency of the externally-applied magnetic field. The frequency response is given by $f_T = (4\omega - 0^2 - \gamma^2)^{1/2}$, and the selected values are larger than those of the steady-state motion.

To understand how the magnetic force acts on paramagnetic materials and causes nanoparticles to move in the z-direction, it is important to understand that the square of the magnetic field gradient is proportional to the magnetic force. Therefore, the motion of magnetic nanoparticles at a given distance is determined by the strength of the magnetic field.

3. Tissue Surface Displacement in an Elastic Medium

The purpose of this section is to derive the force-displacement relationship by using the theory of elasticity for a nanoparticle embedded in elastic half-space. The force on the nanoparticle is applied normal to the boundary of a semi-infinite elastic medium, and solutions were obtained using Galerkin's vector and Mindlin's theory for a point force in a semi-infinite medium [27]. An analysis of the surface displacement of iron-laden tissue is required for a quantitative analysis of the response of an elastic medium to an externally applied magnetic force.

The well-known basic elasticity equation is given by [28]

$$G\left(\nabla^2 + \frac{1}{1-2\nu}\nabla div\right)\rho + K = 0, \tag{18}$$

where K is the body force, G is the modulus of rigidity (shear modulus), ρ is the displacement vector, and is Poisson's ratio for the elastic medium. The displacement using Westergaard's form of the Galerkin vector **F**
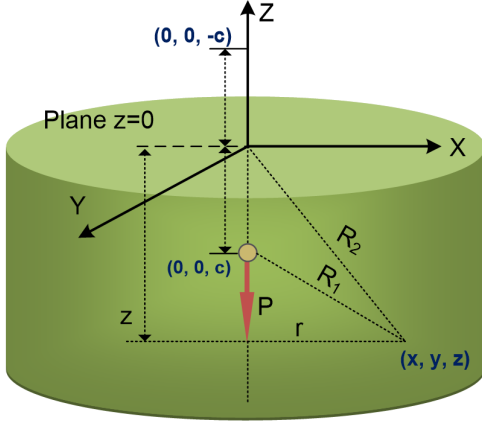
Fig. 6. (Color online) Symmetrical cylindrical coordinates for the semi-infinite elastic model. A vertical force (P) in the interior of the elastic model is applied at point (0, 0, c) in the positive z-direction with $R_1 = \sqrt{(r^2 + (z-c)^2)} + \sqrt{(r^2 + (z+c)^2)}$.

is given by the following:

$$2G\rho = (c\nabla^2 - \nabla div)\mathbf{F},$$
$$\rho = \frac{(c\nabla^2 - \nabla div)\mathbf{F}}{2G}, \tag{19}$$

$\mathbf{F}$ is a vector function that can be expressed as $\mathbf{F} = iX + jY + kZ$, where i, j, and k are unit vectors in the x, y, and z directions, respectively. The displacement equation using Galerkin vector components becomes

$$\left(\nabla^2 + \frac{1}{1-2\nu}\nabla div\right)(c\nabla^2 - \nabla div)\mathbf{F} + 2K = 0. \tag{20}$$

Equation (20) can be expressed as the following:

$$\left(c\nabla^4 - \nabla^2\nabla div + \frac{c}{1-2\nu}\nabla div\nabla^2\right.$$
$$\left. - \frac{1}{1-2\nu}\nabla div\nabla div\right)\mathbf{F} + 2K = 0. \tag{21}$$

with $\nabla^4 = \nabla^2\nabla div = \nabla div\nabla div$. The reduced displacement equation, Eq. (22), will be satisfied by the equation $\left(-1 + \frac{c}{1-2\nu} - \frac{1}{1-2\nu}\right) = 0$, which then becomes the following:

$$\left[c\nabla^4 + \nabla^2\nabla div\left(-1 + \frac{c}{1-2\nu} - \frac{1}{1-2\nu}\right)\right]\mathbf{F}$$
$$+ 2K = 0. \tag{22}$$

Therefore, the basic displacement equation (19) in elastic media using c = 2(1 − ν) can be express as follows:

$$2G\rho = [2(1-\nu)\nabla^2 - \nabla div]\mathbf{F}. \tag{23}$$

In Eq. (22), we may obtain $2(1-\nu)\nabla^4\mathbf{F} = -2\mathbf{K}$ and $\nabla^4\mathbf{F} = -\frac{\mathbf{K}}{(1-\nu)}$.

$\mathbf{K}$ is defined as the body force in equation (23), which can be restated as:

$$\begin{aligned} 2Gu &= 2(1-\nu)\nabla^2\mathbf{X} - \nabla div\mathbf{F} \\ &= 2(1-\nu)\nabla^2\mathbf{X} - \nabla\nabla\cdot\mathbf{F}, \\ 2Gv &= 2(1-\nu)\nabla^2\mathbf{Y} - \nabla div\mathbf{F} \\ &= 2(1-\nu)\nabla^2\mathbf{Y} - \nabla\nabla\cdot\mathbf{F}, \\ 2Gw &= 2(1-\nu)\nabla^2\mathbf{Z} - \nabla div\mathbf{F} \\ &= 2(1-\nu)\nabla^2\mathbf{Z} - \nabla\nabla\cdot\mathbf{F}. \end{aligned} \tag{24}$$

Equation (25) also gives another representation, as indicated below:

$$\begin{aligned} 2Gdiv\rho &= div[2(1-\nu)\nabla^2 - \nabla div]\mathbf{F} \\ &= [2(1-\nu)\nabla^2 div - \nabla^2 div]\mathbf{F} \\ &= (1-2\nu)\nabla^2 div\mathbf{F}. \end{aligned} \tag{25}$$

A vertical force P applied at a distance below the plane surface z = 0 in an elastic medium is shown in Fig. 6 [27].

Combining a sequence of Galerkin vectors defining a nucleus of stress and strain [29] produces seven components comprised of parts $z_1, \ldots z_7$, which are defined as the following:

$$z_1 = \frac{P}{8\pi(1-\nu)}R_1, \qquad z_2 = -\frac{P}{8\pi(1-\nu)}R_2,$$
$$z_3 = -\frac{Pc}{4\pi(1-\nu)}\frac{(z+c)}{R_2}, \qquad z_4 = \frac{P}{2\pi}R_2,$$
$$z_5 = \frac{(1-2\nu)P}{2\pi}[(z+c)\log(R_2+z+c) - R_2],$$
$$z_6 = -\frac{(1-2\nu)Pc}{2\pi(1-\nu)}[\log(R_2+z+c)],$$
$$z_7 = \frac{Pc^2}{4\pi(1-\nu)}\frac{1}{R_2}, \quad \text{with}$$
$$\mathbf{F} = z_1 + z_2 + z_3 + z_4 + z_5 + z_6 + z_7. \tag{26}$$

If a point source position c approaches zero corresponding to a single force applied at the surface of the boundary, the solution becomes a Boussineq's equation $\mathbf{F}_B$, using the Galerkin vector $\mathbf{F}$, as follows:

$$\mathbf{F}_B = \frac{P}{2\pi}[2\nu R + (1-2\nu)z\log(R+z)]. \tag{27}$$

In Eq. (26), with the z_1 component representing the well-known Kevin's single force solution in a medium with infinite extent, $c \to \infty$, the corresponding Galerkin vector $\mathbf{F}$ for the Kelvin solution $\mathbf{F}_k$ becomes the following:

$$\mathbf{F}_k = \mathbf{k}\left[\frac{PR_1}{8\pi(1-\nu)}\right]. \tag{28}$$

As a result, the solution for vertical displacement, which is normal to the boundary, in elastic media obtained by combining seven nuclei of stress and strain for Eq. (26) becomes

$$F = \left[\frac{P\mathbf{k}}{8\pi(1-\nu)}\right] \left\{ \begin{array}{l} R_1 + (8\nu(1-\nu)-1)R_2 + \\ 4(1-2\nu)[(1-\nu)z - \nu c]\log(R_2 + z + c) - \frac{2cz}{R_2} \end{array} \right\}. \tag{29}$$

After Eq. (24) is transformed to cylindrical coordinates, the displacement, which will only be observed in the z-direction, is

$$W = \left(\frac{1}{2G}\right)[2(1-\nu)\nabla^2\mathbf{Z} - \nabla div\mathbf{F}] = \left(\frac{1}{2G}\right)\left[2(1-\nu)\Delta\mathbf{Z} - \frac{\partial^2 Z}{\partial z^2}\right]. \tag{30}$$

The displacement in elastic media in cylindrical coordinates then becomes

$$W = \left[\frac{P}{16\pi G(1-\nu)}\right] \left\{ \begin{array}{l} \frac{3-4\nu}{R_1} + \frac{8\nu^2 - 12\nu + 5}{R_2} + \frac{(z-c)^2}{R_1^3} \\ + \frac{(3-4\nu)(z+c)^2 - 2cz}{R_2^3} + \frac{6cz(z+c)^2}{R_2^5} \end{array} \right\}, \tag{31}$$

with Young's modulus $E = 2(1+\nu)G$ and the shear modulus G.

In the deviation of the displacement defined by Eq. (31), an analysis of the surface displacement of the iron-laden tissue due to an applied magnetic force that acts on superficial samples with magnetic nanoparticles embedded would be useful:

$$\ddot{z}_{np}(t) = \frac{a\left[\begin{array}{l} \omega_B^3\gamma\sin(\omega_B t)\omega_0^2 + \cos(\omega_B t)\omega_B^2\omega_0^4 - \cos(\omega_B^4\omega_0^2) + \\ \frac{1}{4}\gamma^2\exp\left(-\frac{1}{2}t\gamma\right)\left(\begin{array}{l} -\omega_B^2(\gamma^2 + \omega_B^2 - \omega_0^2)\cosh\left(\frac{1}{2}t(\gamma^2 - 4\omega_0^2)^{\frac{1}{2}}\right) - \\ \frac{\omega_B^2\gamma(-3\omega_0^2 + \omega_b^2 + \gamma^2)\sinh\left(\frac{1}{2}t(\gamma^2 - 4\omega_0^2)^{\frac{1}{2}}\right)}{(\gamma^2 - 4\omega_0^2)^{\frac{1}{2}}} \end{array}\right) - \\ \gamma\exp\left(-\frac{1}{2}t\gamma\right)\left(-\frac{1}{2}\omega_B^2(\gamma^2 + \omega_B^2 - \omega_0^2)\right)\sinh\left(\frac{1}{2}t(\gamma^2 - 4\omega_0^2)^{\frac{1}{2}}\right)(\gamma^2 - 4\omega_0^2)^{\frac{1}{2}} \\ -\frac{1}{2}\omega_B^2\gamma(-3\omega_0^2 + \omega_B^2 + \gamma^2)\cosh\left(\frac{1}{2}t(\gamma^2 - 4\omega_0^2)^{\frac{1}{2}}\right) \\ +\exp\left(-\frac{1}{2}t\gamma\right)\left(-\frac{1}{4}\omega_B^2(\gamma^2 + \omega_B^2 - \omega_0^2)\right)\cosh\left(\frac{1}{2}t(\gamma^2 - 4\omega_0^2)^{\frac{1}{2}}\right)(\gamma^2 - 4\omega_0^2) \\ -\frac{1}{4}\omega_B^2\gamma(-3\omega_0^2 + \omega_B^2 + \gamma^2)\sinh\left(\frac{1}{2}t(\gamma^2 - 4\omega_0^2)^{\frac{1}{2}}\right)(\gamma^2 - 4\omega_0^2)^{\frac{1}{2}} \end{array}\right]}{(\omega_0^2(\gamma^2\omega_B^2 - 2\omega_B^2\omega_0^2 + \omega_B^4 + \omega_0^4))}. \tag{32}$$

Finally, the tissue's surface displacement due to nanoparticles embedded in elastic media, $z_s(t)$, when combined with $F = ma = m\ddot{z}_{np}$, becomes

$$z_s(t) = \left[\frac{m\ddot{z}_{np}}{16\pi G(1-\nu)}\right] \left\{ \begin{array}{l} \frac{3-4\nu}{R_1} + \frac{8\nu^2 - 12\nu + 5}{R_2} + \frac{(z-c)^2}{R_1^3} \\ + \frac{(3-4\nu)(z+c)^2 - 2cz}{R_2^3} + \frac{6cz(z+c)^2}{R_2^5} \end{array} \right\}. \tag{33}$$

Figure 7 shows simulation result derived from Eq. (33) and the corresponding experimental result. Figure 7(a) shows the simulation result for tissue surface displacement in iron-laden elastic media obtained using Eq. (33) with a magnetic field input (1 Tesla at 2 Hz) for the case of a force normal to the boundary (c = 0.5 mm, $\nu = 0.4$, and G = 100), where G is the shear modulus and E is Young's module expressed by relationship, $E = 2(1 + \nu)G$. Figure 7(b) illustrates the result of the iron-laden tissue displacement using a DP-OCT system to measure the surface displacement due to the application of a magnetic force to nanoparticles in elastic media.

IV. DISCUSSION

The tissue surface displacement due to an externally applied magnetic field consists of two motions, transient and steady state, from simulation data and experimental data, as shown in Figs. 7(a) and (b). After a transient response, the physical displacement approaches a steady-state response that resembles the input sinusoidal signal. All experimental data for the steady state show that the frequency response of tissue's surface displacement from iron-laden macrophages was exactly twice the exciting frequency of the input magnetic field as shown in Figs. 5
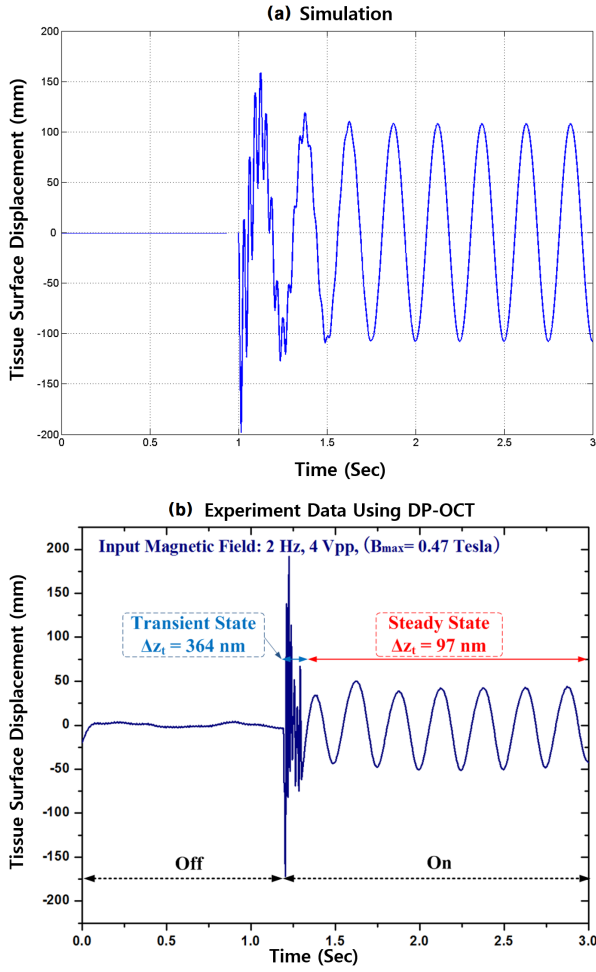
Fig. 7. (Color online) (a)Simulation results for tissue surface displacement (Δz_s) as in the experimental setup. (b) Tissue surface displacement (Δz_s) in iron-laden liver specimens due to nanoparticle movement in response to a focused magnetic field with a 2 Hz input for rabbit aorta with a MION dose of 0.2 mmol Fe/kg using. The experimental data was acquired by using an applied DP-OCT and applied maximum magnetic flux density of 0.47 Tesla.

and 7. The motion of the nanoparticles at double the modulation frequency originates from the magnetic force being proportional to the product of the magnetic flux density and the gradient from Eq. (6). The amplitude of the tissue's surface displacement in the steady state may depend on the magnetic field and its gradient as $a = \frac{\chi_s V_s}{2m\mu_0}\mathbf{B}_z(0)\frac{\partial \mathbf{B}_z(0)}{\partial z}$. In Eq. (10), the maximum amplitude of the nanoparticle displacement at steady state occurs when $\omega_B^2 = \omega_0^2 - \frac{\gamma^2}{2}$. Alternatively, when $\omega_0 \gg \omega_B$, the amplitude of movement diminishes to zero. The variation in the amplitude of tissue's surface displacement ($z_s(t)$) by applying a sweep frequency may be associated with the spatial variations of viscoelastic tissue properties (γ, ω_0) in different specimens. Further experimental studies and mathematical simulations will be required to evaluate the spatial variations of γ and ω_0. The quantitative interpretation of the tissue's surface displacement ($z_s(t)$) in specimens containing different sizes of magnetic nanoparticles will require further study and necessitate a mathematical model incorporating viscoelastic properties of tissue. Furthermore, a mathematical model incorporating the viscoelastic properties of tissue will allow a quantitative analysis of tissue displacement in iron-laden specimens for high-risk plaque lesions.

Our results suggest that DP-OCT, with nanometer resolution, may allow detection of iron-laden macrophages at relatively low doses of MION nanoparticles in vulnerable atherosclerotic plaque lesions, which was confirmed by histological findings (results not shown).

V. CONCLUSION

In conclusion, the frequency response of tissue movement in response to an externally- applied magnetic field was twice the stimulus frequency, which is consistent with established magneto-dynamic principles. Increasing the magnetic-field strength increased surface displacement of the specimens. In saline control specimens, no significant tissue surface displacement ($z_s(t)$) was observed in response to an externally-applied magnetic field in both liver and aorta specimens. The results of our experiments suggest that magneto-motive DP-OCT is a promising technique for detecting of macrophages with magnetic nanoparticles for molecular imaging applications in patients with cardiovascular disease.

ACKNOWLEDGMENTS

REFERENCES

[1] Y. X. Wang, S. M. Hussain and G. P. Krestin, Eur. Radiol. **11**, 2319 (2001).
[2] C. W. Lu *et al.*, Nano. Lett. **7**, 149 (2007).
[3] J. A. Frank, B. R. Miller, A. S. Arbab, H. A. Zywicke, E. K. Jordan, B. K. Lewis, L. H. Bryant, Jr. and J. W. Bulte, Radiology. **228**, 480 (2003).
[4] A. S. Lubbe, C. Alexiou and C. Bergemann, J. Surg. Res. **95**, 200 (2001).
[5] T. M. Said, S. Grunewald, U. Paasch, M. Rasch, A. Agarwal and H. J. Glander, Fertil. Steril. **83**, 1442 (2005).
[6] P. Wunderbaldinger, L. Josephson and R. Weissleder, Bioconjug. Chem. **13**, 264 (2002).
[7] V. S. Kalambur, B. Han, B. E. Hammer, T. W. Shield and J. C. Bischof, Nanotechnology. **16**, 1221 (2005).

[8] J. Kim, J. Oh, T. E. Milner and J. S. Nelson, Nanotechnology **18**, 035504 (2007).

[9] J. Oh, M. D. Feldman, J. Kim, H. W. Kang, P. Sanghi and T. E. Milner, Lasers in surgery and medicine **39**, 266 (2007).

[10] J. Oh, M. D. Feldman, J. Kim, C. Condit, S. Emelianov and T. E. Milner, Nanotechnology **17**, 4183 (2006).

[11] J. Kim, J. Oh and B. Choi, Journal of biomedical optics **15**, 011110 (2010).

[12] C. W. Wei, J. Xia, I. Pelivanov, C. Jia, S. W. Huang, X. Hu, X. Gao and M. O'Donnell, Journal of biophotonics **6**, 513 (2013).

[13] M. Evertsson, P. Kjellman, M. Cinthio, S. Fredriksson, R. in't Zandt, H. Persson and T. Jansson, IEEE. Trans. Ultrason. Ferroelectr. Freq. Control. **61**, 1276 (2014).

[14] C. W. Wei, J. Xia, I. Pelivanov, C. Jia, S. W. Huang, X. Hu, X. Gao and M. O'Donnell, J. Biophotonics. **6**, 513 (2013).

[15] J. Kim, A. Ahmad and S. A. Boppart, Opt. Express. **21**, 7139 (2013).

[16] J. Kim, J. Oh and T. E. Milner, J. Biomed. Opt. **11**, 041122 (2006).

[17] D. L. Thorek, A. K. Chen, J. Czupryna and A. Tsourkas, Ann. Biomed. Eng. **34**, 23 (2006).

[18] J. F. Schenck, J. Magn. Reson. Imaging. **12**, 2 (2000).

[19] J. W. Bulte, R. A. Brooks, B. M. Moskowitz, L. H. Bryant, Jr. and J. A. Frank, Magn. Reson. Med. **42**, 379 (1999).

[20] K. E. Kellar, D. K. Fujii, W. H. Gunther, K. Briley-Saebo, A. Bjornerud, M. Spiller and S. H. Koenig, J. Magn. Reson. Imaging. **11**, 488 (2000).

[21] T. Shen, R. Weissleder, M. Papisov, A. Bogdanov, Jr. and T. J. Brady, Magn. Reson. Med. **29**, 599 (1993).

[22] C. Z. Simonsen, L. Ostergaard, P. Vestergaard-Poulsen, L. Rohl, A. Bjornerud and C. Gyldensted, J. Magn. Reson. Imaging. **9**, 342 (1999).

[23] R. M. Weisskoff and S. Kiihne, Magnet. Reson. Med. **24**, 375 (1992).

[24] Q. A. Pankhurst, J. Connolly, S. K. Jones and J. Dobson, J. Phys. D: Appl. Phys. **36**, R167 (2003).

[25] R. Weissleder, A. S. Lee, B. A. Khaw, T. Shen and T. J. Brady, Radiology. **182**, 381 (1992).

[26] R. Weissleder, A. S. Lee, A. J. Fischman, P. Reimer, T. Shen, R. Wilkinson, R. J. Callahan and T. J. Brady, Radiology. **181**, 245 (1991).

[27] R. D. Mindlin, physics. **7**, 195 (1936).

[28] H. M. Westergaard, Theory of elasticity and plasticity (Harvard university press, Cambrige, 1952).

[29] R. D. Mindlin and D. H. Cheng, J. Appl. Phys. **21**, (1950).

[30] P. F. Hahn, D. D. Stark, J. M. Lewis, S. Saini, G. Elizondo, R. Weissleder, C. J. Fretz and J. T. Ferrucci, Radiology. **175**, 695 (1990).

[31] T. Bach-Gansmo, Acta. Radiol. Suppl. **387**, 1 (1993).

[32] P. Reimer and B. Tombach, Eur. Radiol. **8**, 1198 (1998).

[33] P. Reimer, E. J. Rummeny, H. E. Daldrup, T. Balzer, B. Tombach, T. Berns and P. E. Peters, Radiology. **195**, 489 (1995).

[34] T. Ichikawa, A. S. Arbab, T. Araki, K. Touyama, H. Haradome, J. Hachiya, M. Yamaguchi, H. Kumagai and S. Aoki, AJR. Am. J. Roentgenol. **173**, 207 (1999).

[35] A. E. Stillman, N. Wilke, D. Li, M. Haacke and S. McLachlan, J. Comput. Assist. Tomogr. **20**, 51 (1996).

[36] W. W. Mayo-Smith, S. Saini, G. Slater, J. A. Kaufman, P. Sharma and P. F. Hahn, AJR. Am. J. Roentgenol. **166**, 73 (1996).

[37] Y. Anzai, J. A. Brunberg and R. B. Lufkin, J. Magn. Reson. Imaging. **7**, 774 (1997).

[38] T. Tanoura, M. Bernas, A. Darkazanli, E. Elam, E. Unger, M. H. Witte and A. Green, AJR. Am. J. Roentgenol. **159**, 875 (1992).

[39] L. Rohl, L. Ostergaard, C. Z. Simonsen, P. Vestergaard-Poulsen, L. Sorensen, A. Bjornerud, K. B. Saebo and C. Gyldensted, Acta. Radiol. **40**, 282 (1999).

[40] R. Guimaraes, O. Clement, J. Bittoun, F. Carnot and G. Frija, AJR. Am. J. Roentgenol. **162**, 201 (1994).